Monthly Notices of the ROYAL ASTRONOMICAL SOCIETY

MNRAS **548,** 1–16 (2026)
Advance Access publication 2026 April 09

https://doi.org/10.1093/mnras/stag674

The broad-band spectral energy distribution of candidate neutrino blazars

Athira M Bharathan [1,2★], C. S. Stalin [3], Markus Böttcher,[2] S. Sahayanathan,[4,5] Blesson Mathew [1] and Subir Bhattacharyya [4,5]

[1]*Department of Physics and Electronics, CHRIST (Deemed to be University), Bangalore, India, 560029*
[2]*Centre for Space Research, North-West University, Potchefstroom 2531, South Africa*
[3]*Indian Institute of Astrophysics, Block II, Koramangala, Bangalore 560 034, India*
[4]*Astrophysical Sciences Division, Bhabha Atomic Research Centre, Mumbai 400085, India*
[5]*Homi Bhabha National Institute, Mumbai 400094, India*

Accepted 2026 April 8. Received 2026 April 7; in original form 2025 February 11

ABSTRACT

Blazars, the jet-dominated class of active galactic nuclei comprising flat-spectrum radio quasars (FSRQs) and BL Lacertae objects (BL Lacs), are now increasingly identified as potential sources of high-energy neutrinos. Such neutrino blazars are ideal targets to investigate the high-energy emission processes and to understand their role as neutrino sources. We report results on four candidate neutrino blazars, PKS 0446+112, TXS 0506+056, PKS 1424−418, and PKS 1502+106. We carried out γ-ray spectral and timing analysis on three time periods that comprise a quiescent epoch, an epoch that corresponds to neutrino detection, and a flaring epoch. We also carried out modelling of the broad-band spectral energy distribution (SED) on those three epochs. We found that the γ-ray spectra of the BL Lac TXS 0506+056 can be adequately described by a power law, while the spectra of the other three FSRQs require a log-parabola model. On shorter time-scales, we observed flux variability with doubling/halving time-scales of 4.70, 9.24, 30.76, and 15.42 h for PKS 0446+112, TXS 0506+056, PKS 1424−418, and PKS 1502+106, respectively. The SEDs of most of the epochs for the sources are well explained by a leptonic scenario. However, the quiescent epoch of PKS 1502+106 and the neutrino-emission epoch of PKS 0446+112 required an additional hadronic component to reproduce the observed SEDs. Our analysis reveals a complex interplay of leptonic and hadronic processes. While certain neutrino-associated epochs align with a leptonic model, others necessitate a hadronic component to explain the emission features.

Key words: galaxies: active – *(galaxies:)* BL Lacertae objects: individual: TXS 0506+056 – galaxies: jets – gamma-rays: general.

1 INTRODUCTION

Blazars, which encompass flat-spectrum radio quasars (FSRQs) and BL Lacertae objects (BL Lacs), are a unique subclass of active galactic nuclei (AGNs) with their highly relativistic jets aligned closely to the line of sight to the observer (R. D. Blandford & M. J. Rees 1978). This separation into FSRQs and BL Lacs is observationally based on the presence of strong (EW $>$ 5 Å) or weak (EW $<$ 5 Å) emission lines in their spectra (J. T. Stocke et al. 1991). A more physical distinction put forward by G. Ghisellini et al. (2011) is based on the ratio of the luminosity of the broad-line region (BLR) (L_{BLR}) to the Eddington luminosity (L_{Edd}) with this ratio larger than 5×10^{-4} for FSRQs, while it is lower than 5×10^{-4} for BL Lacs. The emission from blazars is dominated by their Doppler boosted non-thermal jet emission. They are known to show flux variations across the electromagnetic spectrum from low-energy radio to high-energy ($E > 100$ MeV) γ-rays, and in some cases even very high-energy TeV γ-rays, on a range of time-scales from minutes to days to months (H. R. Miller, M. T. Carini & B. D. Goodrich 1989; J. C. Noble & H. R. Miller 1994; S. J. Wagner & A. Witzel 1995; M.-H. Ulrich, L. Maraschi & C. M. Urry 1997; T. P. Dominici et al. 2004; P. Kushwaha et al. 2018; G. Bhatta 2021; V. V. Vlasyuk et al. 2024; M. S. Butuzova et al. 2025). In addition to flux variations, they are highly polarized (J. R. P. Angel & H. S. Stockman 1980; A. M. Bharathan et al. 2024a, c) and are also known to show polarization variations in the radio (J.-H. Fan et al. 2008), optical (S. Rakshit et al. 2017; A. Pandey, B. Rajput & C. S. Stalin 2022; B. Rajput et al. 2022), and X-ray energies (X.-K. Hu et al. 2024; P. M. Kouch et al. 2024).

Blazars exhibit distinctive spectral energy distributions (SEDs). When represented in the usual $\log\nu f(\nu)$ versus $\log\nu$ format, the SED displays two prominent broad humps. The low-energy component is observed to peak in the infrared-optical energy range (and in some cases in the X-ray energy range), which is attributed to synchrotron emission from relativistic electrons

★ E-mail: athira.bharathan@res.christuniversity.in

Table 1. The details of blazars associated with neutrino detections selected for detailed analysis. Here, T_0 is the time in MJD of the neutrino detection, and Reference points to the article that reported the neutrino detection.

Source	Class	RA (h:m:s)	Dec. (d:m:s)	z	IceCube Alert	T_0 (MJD)	Energy (TeV)	Reference
PKS 0446+112	FSRQ	04:49:07.6711	+11:21:28.596	2.15	240105A	60 314	1.1	IceCube Collaboration (2024)
TXS 0506+056	BL Lac	05:09:25.9644	+05:41:35.333	0.34	170922A	58 018	290	IceCube Collaboration (2018a)
PKS 1424−418	FSRQ	14:27:56.2975	−42:06:19.437	1.52	121 204	56 265	2000	M. G. Aartsen et al. (2014)
PKS 1502+106	FSRQ	15:04:24.9797	+10:29:39.198	1.84	190730A	58 694	300	I. Taboada & R. Stein (2019)

spiraling around the magnetic field lines in the jet. Based on the frequency of the synchrotron peak (ν_{syn}), blazars are further subdivided into three different classes: high, intermediate, and low synchrotron peaked (HSP, ISP, and LSP, respectively) blazars, depending on whether $\nu_{syn} > 10^{15}$ Hz, 10^{14} Hz $< \nu_{syn} < 10^{15}$ Hz, or $\nu_{syn} < 10^{14}$ Hz (A. A. Abdo et al. 2010b). While the low-energy hump is well understood to be of electron synchrotron origin as evidenced through the observed high optical and radio polarization (R. Scarpa & R. Falomo 1997; P. S. Smith et al. 2007), the origin of the high-energy component that peaks in the MeV − GeV energy range is debated between leptonic and hadronic processes.

In the leptonic scenario, the radiative output across the electromagnetic spectrum is primarily attributed to leptons (electrons and positrons), while any protons in the jet are assumed not to be accelerated to energies high enough to significantly impact the radiative output. In this process, the high-energy emission is produced through inverse Compton scattering, wherein the low-energy photons are Compton up scattered by the same relativistic electrons that produce synchrotron emission at lower energies. The seed photons could be internal to the jet, i.e. the synchrotron photons from the jet through a process called synchrotron self-Compton (SSC; A. Konigl 1981; A. P. Marscher & W. K. Gear 1985; G. Ghisellini & L. Maraschi 1989), or photons external to the jet, such as the accretion disc (C. D. Dermer & R. Schlickeiser 1993), the BLR (M. Sikora, M. C. Begelman & M. J. Rees 1994; G. Ghisellini & P. Madau 1996), and the torus (M. Błażejowski et al. 2000; G. Ghisellini & F. Tavecchio 2008), a process called external Compton (EC; M. C. Begelman & M. Sikora 1987; F. Melia & A. Konigl 1989; C. D. Dermer, R. Schlickeiser & A. Mastichiadis 1992). In this scenario, one expects to see a close correlation between optical and GeV flux variations since the same population of electrons is responsible for the emission at both the low-energy and high-energy bands. Such correlations supporting the leptonic scenario are seen in multiwavelength observations of flaring blazars (I. Liodakis et al. 2018, 2019). However, recent studies concentrating on a systematic investigation of the correlation between optical and GeV flux variations of a large sample of blazars (B. Rajput et al. 2019, 2021) have lead to (a) instances of close correlation between optical and GeV flux variations, (b) instances of optical flare without a GeV counterpart, and (c) instances of GeV flare without an optical counterpart. These observations (see also T. Jaeger et al. 2023) suggest the high-energy component to have contributions from more than one process.

In contrast to the leptonic process, the hadronic model attributes the high-energy emission to processes involving relativistic protons. In this scenario, the emission can result from synchrotron radiation produced by protons as they spiral in the magnetic field, or from interactions that lead to photon-pion production (K. Mannheim & P. L. Biermann 1992; K. Mannheim 1993; M. Böttcher et al. 2013). These interactions may result in the generation of very high-energy γ-rays and secondary particles such as neutrinos, which are unique signatures of hadronic processes. In this scenario, the correlation between optical − GeV flux variations may not be expected. The recent detection of neutrinos coincident with flaring blazars such as TXS 0506+056 (P. Padovani et al. 2018), 3HSP J095507.9+355101 (P. Giommi et al. 2020b) suggests that blazar jets are possible emitters of high-energy neutrinos (P. Giommi et al. 2020a) and the high-energy component in blazar SEDs can have contributions from processes that also involve hadrons. Current observations show that a very small fraction of AGNs (say $<$ 1 per cent) are neutrino emitters (R. Abbasi et al. 2023). While blazar SEDs can be equally well represented by leptonic and hadronic models (M. Böttcher et al. 2013), direct proof of hadronic interactions from blazar jet is through observation of neutrinos. Yet, another potential way to distinguish between leptonic and hadronic origin of high-energy emission from blazars is through observations of X-ray and γ-ray polarization, which are different for leptonic and hadronic models (H. Zhang & M. Böttcher 2013; H. Zhang, M. Böttcher & I. Liodakis 2024).

Observations with IceCube (M. G. Aartsen et al. 2017) have revealed several spatial associations between high-energy neutrinos and γ-ray loud blazars, strengthening the case for hadronic interactions in relativistic jets (M. Kadler et al. 2016; S. Garrappa et al. 2019; A. Franckowiak et al. 2020; P. Giommi et al. 2020a; S. Buson et al. 2022, 2023; N. Sahakyan et al. 2023). Yet, the relative importance of leptonic and hadronic processes in powering the broad-band SEDs of blazars remains a subject of debate. Individual case studies illustrate this ambiguity. For example, the neutrino-associated blazar PKS 0735+178 was found to be well described by a leptonic model during the neutrino detection epoch, even though the neutrino association itself implies that hadronic channels cannot be excluded (A. M. Bharathan et al. 2024b). This highlights a broader challenge; blazars may not all behave in the same way, and the hadronic contribution can be strongly source and epoch-dependent. A recent population-level analysis by X. Rodrigues et al. (2024) provides a useful perspective of modelling a large sample of 324 *Fermi*-Large Area Telescope (LAT) blazars. They showed that in roughly one-third of their sample of sources, the X-ray spectra favour an additional component from hadronic interactions, whereas in the remaining two-thirds, a leptonic model suffices. The corresponding neutrino output from the population accounts for about 20 per cent of the diffuse IceCube flux, consistent with current stacking limits. Against this backdrop, our work complements the population results by presenting detailed time-resolved modelling of four blazars associated with IceCube neutrinos. By focusing on multi-epoch SEDs, we explore whether the relative leptonic–hadronic balance changes across flux states and how such variability might connect to neutrino production. In this paper, we present the results of our study on four blazars: PKS 0446+112, TXS 0506+056, PKS 1424−418, and PKS 1502+106 that are found to be associated with IceCube neutrinos. The choice of

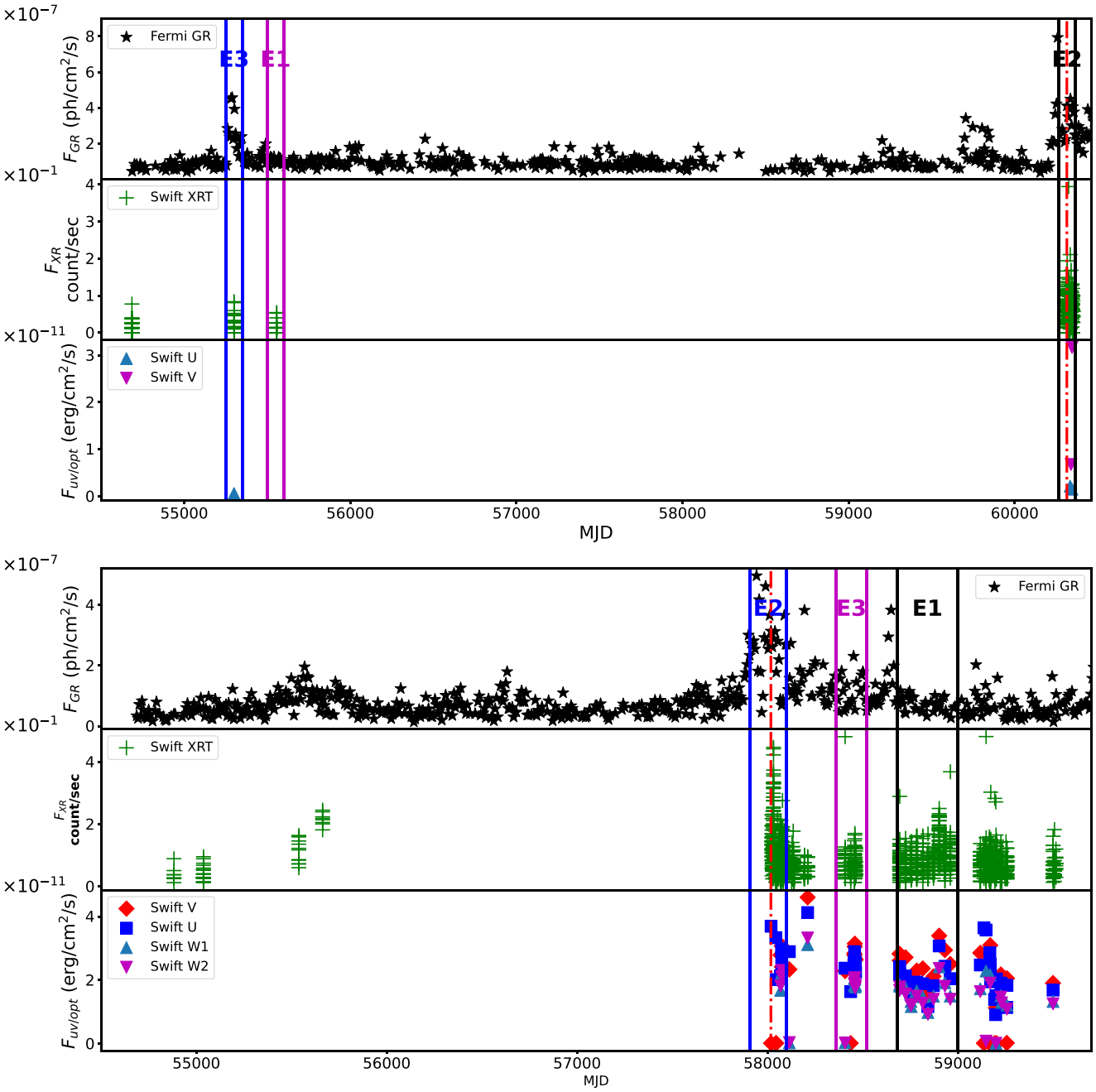

Figure 1. Multiwavelength light curves for the sources PKS 0446+112 (top panel) and TXS 0506+056 (bottom panel). In each of the panels, the upper, middle, and lower plots show the γ−ray, X-ray, and optical/UV light curves in $W1$, $W2$, U, and V filters. The dot–dashed lines refer to the epoch of neutrino detection.

these four blazars is based on the availability of multiwavelength data.

PKS 0446+112 is a γ-ray bright FSRQ (4FGL J0449+1121) located at a redshift of $z = 2.153$ (S. Paiano et al. 2024) and powered by a black hole of mass $\sim 7.9 \times 10^7$ M$_\odot$ (M. S. Shaw et al. 2012). It is highly luminous in γ-rays ($E >$ 100 MeV) with a value of 1.21 $\times$ 10^{48} erg s^{-1} (N. Sahakyan et al. 2024b). It was reported to be spatially coincident with the IceCube event IC-240105 (IceCube Collaboration 2024) with an estimated energy of 1.1 TeV. Its time averaged broad-band SED has been modelled with a one zone leptonic scenario, with the X-ray and γ-ray emission being attributed to inverse Compton processes (N. Sahakyan et al. 2024b).

TXS 0506+056 at a redshift of $z = 0.3365$ (S. Paiano et al. 2018) is a radio-bright and a flaring γ-ray blazar (P. Padovani et al. 2018) found to be associated with a 290 TeV neutrino alert, IceCube-170922A by IceCube on 2017 September 22 (IceCube Collaboration 2018b). Analysis of archival data prior to this alert has revealed an excess of neutrinos detected towards the direction of TXS 0506+056 during the years 2014−2015. However, during this period, the source did not exhibit increased activity in the radio,

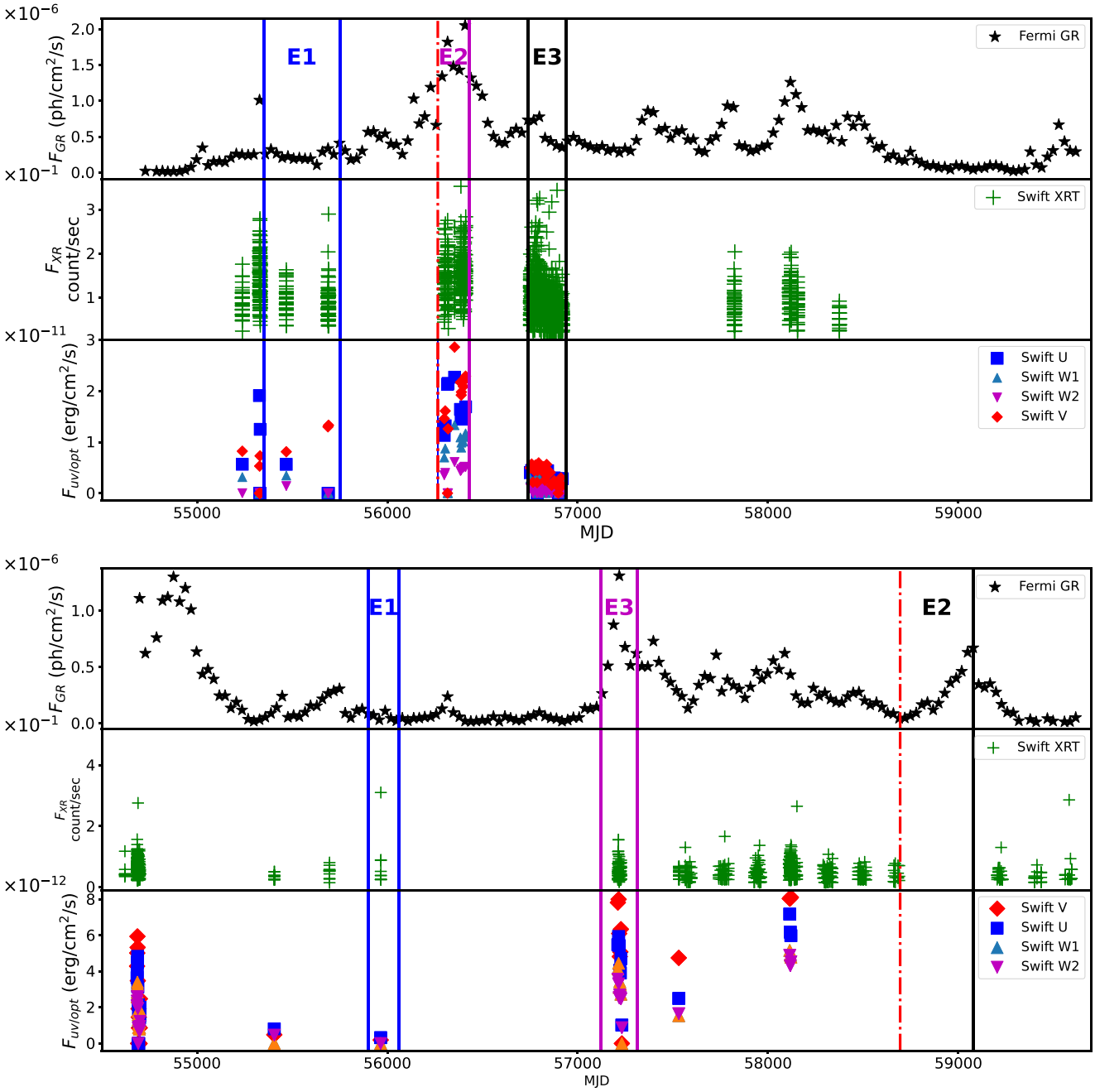

Figure 2. Multiwavelength light curves for the sources PKS 1424−418 (top panel) and PKS 1502+106 (bottom panel). The other descriptions are same as in Fig. 1.

optical, or γ-ray energies (IceCube Collaboration 2018a). These observations led to identify the γ-ray blazar TXS 0506+056 as the first extragalactic counterpart to a neutrino event. Also, neutrino events associated with the blazar occurred in 2021−2022 and 2022−2023. The SED of the source during all the four neutrino detection epochs were well reproduced with a stochastic dissipation model (Z.-J. Wang et al. 2024) that also explains the episodic neutrino emission from TXS 0506+056.

PKS 1424−418 is an FSRQ at a redshift of $z = 1.522$ (M. T. Murphy et al. 2019). It is listed in the 4FGL catalogue with the identifier 4FGL J1427.9-4206 (S. Abdollahi et al. 2020), and is powered by a black hole of mass 4.5×10^9 $M_\odot$ (Z.-H. Fan & X. Cao 2004). It is variable in γ-rays, optical, infrared (J. Abhir et al. 2021), and sub-mm (D.-W. Kim et al. 2024). It has an extended one-sided morphology in the radio (P. Benke et al. 2024) and is the most distant TeV-detected blazar associated with an IceCube alert. It was found to be spatially coincident with the IceCube alert IC 121204, which had an estimated energy of 2 PeV, detected on 2012 December 4 (M. G. Aartsen et al. 2014). Broad-band SED modelling carried out on the source at two flaring epochs found the emission to be well described by a leptonic scenario (J. Abhir et al. 2021).

PKS 1502+106 (4FGL J1504.4+1029), an FSRQ situated at a redshift of $z = 1.8378$ (P. C. Hewett & V. Wild 2010), was consid-

ered a promising neutrino source candidate in the catalogue of M. G. Aartsen et al. (2020). It hosts a black hole of mass 4.4×10^9 $M_\odot$ (Y. Shen et al. 2011). It was found to coincide with the IceCube alert IC 190730A (I. Taboada & R. Stein 2019), with an estimated energy of 300 TeV. While the source is not very bright in γ-rays during the epoch of neutrino detection, it was bright in the radio band (S. Kiehlmann et al. 2019). It is variable in the optical (T. Morton et al. 2008) and γ-ray energies (A. A. Abdo et al. 2010a). However, no significant excess in γ-ray emission was observed during the IceCube event (IceCube-190730A). According to X. Rodrigues et al. (2021), the emission from the source during its quiescent and flaring states can be described by a hadronic model. A summary of the sources investigated in this study is given in Table 1.

This paper is organized as follows. Section 2 details the multiwavelength data and reduction procedures, the analysis and results are given in Section 3 followed by the discussion and summary in the final section. Throughout this paper we used the cosmological constants $\Omega_M = 0.3$, $\Omega_\Lambda = 0.7$, and $H_0 = 70$ km s^{-1}Mpc^{-1}.

2 MULTIWAVELENGTH DATA AND REDUCTION

We analysed the publicly available data in the γ-ray, X-ray, optical, and ultraviolet (UV) bands from 2008 August to 2022 February, spanning nearly 14 yr for all the sources except PKS 0446+112 for which we used the data from 2008 August to 2024 May in order to cover the period of the most recent IceCube alert on 2024 January 5, ensuring any contemporaneous γ-ray activity is accounted for. Use of such a data set will offer insights into the long-term behaviour of the sources as well as understand the processes that are responsible for their multiwavelength emission.

2.1 γ-ray

In the γ-ray band, we used the data from the LAT (W. B. Atwood et al. 2009) on the *Fermi Gamma-ray Space Telescope*. The *LAT* is a pair-conversion telescope sensitive to γ-ray energies from 20 MeV to over 300 GeV. Operating in scanning mode, *Fermi* covers the entire sky approximately every 3 h. For the sources TXS 0506+056, PKS 1424−418, and PKS 1502+106 we used data from 2008 August to 2022 February (MJD: 54500−59500; ∼170 months), while for PKS 0446+112 we used data from 2008 August to 2024 May (MJD: 54500−60460; ∼190 months). We followed the recommended selection criteria and analysis cuts for PASS8 data using the *Fermi* Science Tools version v10r0p5.[1] Photon-like events were filtered with the criteria 'evclass=128, evtype=3', selecting γ-rays with energies between 0.1 and 300 GeV from a circular region of interest (ROI) with a 15° radius centred on each source. We used a zenith angle cut of 90° to minimize contamination from Earth's limb. For background models, we used the latest isotropic model 'iso_P8R2_SOURCE_V6_v06' and the Galactic diffuse emission model 'gll_iem_v06'. We considered a source to be detected if the test statistic (TS) exceeded 4, corresponding to a 2σ detection significance (J. R. Mattox et al. 1996). We generated weekly time binned light curves, and sources with TS $<$ 4 were classified as undetected for that time bin.

[1] http://fermi.gsfc.nasa.gov/ssc/data/analysis/documentation/

Table 2. Details of the epochs considered for timing, spectral, and SED analysis. Here, Quiet refers to the faint state, Neutrino refers to the epoch when neutrino was detected, and Flare refers to the epoch when the source was in a flaring state.

Source	Epoch	State	MJD start	MJD end	Duration (d)
PKS 0446+112	E_1	Quiet	55500	55600	100
	E_2	Neutrino	60265	60365	100
	E_3	Flare	55250	55350	100
TXS 0506+056	E_1	Quiet	58680	59000	320
	E_2	Neutrino	57910	58100	190
	E_3	Flare	58360	58520	160
PKS 1424−418	E_1	Quiet	55350	55750	400
	E_2	Neutrino	56265	56430	165
	E_3	Flare	56740	56940	200
PKS 1502+106	E_1	Quiet	55900	56060	160
	E_2	Neutrino	58594	58795	200
	E_3	Flare	57120	57135	195

Table 3. Results of γ-ray variability analysis.

Source	Epoch	F_{var}(per cent)
PKS 0446+112	E_1	—
	E_2	15.5 ± 11.8
	E_3	37.1 ± 5.0
TXS 0506+056	E_1	—
	E_2	41.0 ± 3.1
	E_3	33.9 ± 6.6
PKS 1424−418	E_1	28.6 ± 2.1
	E_2	16.3 ± 1.1
	E_3	31.7 ± 1.7
PKS 1502+106	E_1	53.4 ± 9.4
	E_2	71.0 ± 1.9
	E_3	45.1 ± 1.5

Table 4. Results of short-term variability during the epoch of very high γ-ray activity.

Source	Epoch	τ (hr)	r (cm)
PKS 0446+112	E_2	4.70	3.70×10^{15}
TXS 0506+056	E_2	9.24	7.47×10^{16}
PKS 1424−418	E_2	30.76	2.63×10^{16}
PKS 1502+106	E_3	15.42	7.04×10^{15}

2.2 X-ray

We utilized data in the 0.3−10 keV band from the *Swift* X-ray Telescope (D. N. Burrows et al. 2005) obtained from the HEASARC archives.[2] For each of the sources, we reduced the data collected during the specified period using default parameter values as recommended by the instrument team. In this work, we employed data acquired in the photon counting mode for both timing and spectral analysis. We used the recent CALDB files from HEASOFT version 6.30 while running the *xrtpipeline*. To extract source spectra we used a circular region with a 60 arcsec radius, while for background spectra we used a 120 arcsec radius circular region. To generate the the exposure map we used the *XIMAGE* tool, and to generate the ancillary response files we used the *xrtmkarf* task.

[2] https://heasarc.gsfc.nasa.gov/docs/archive.html

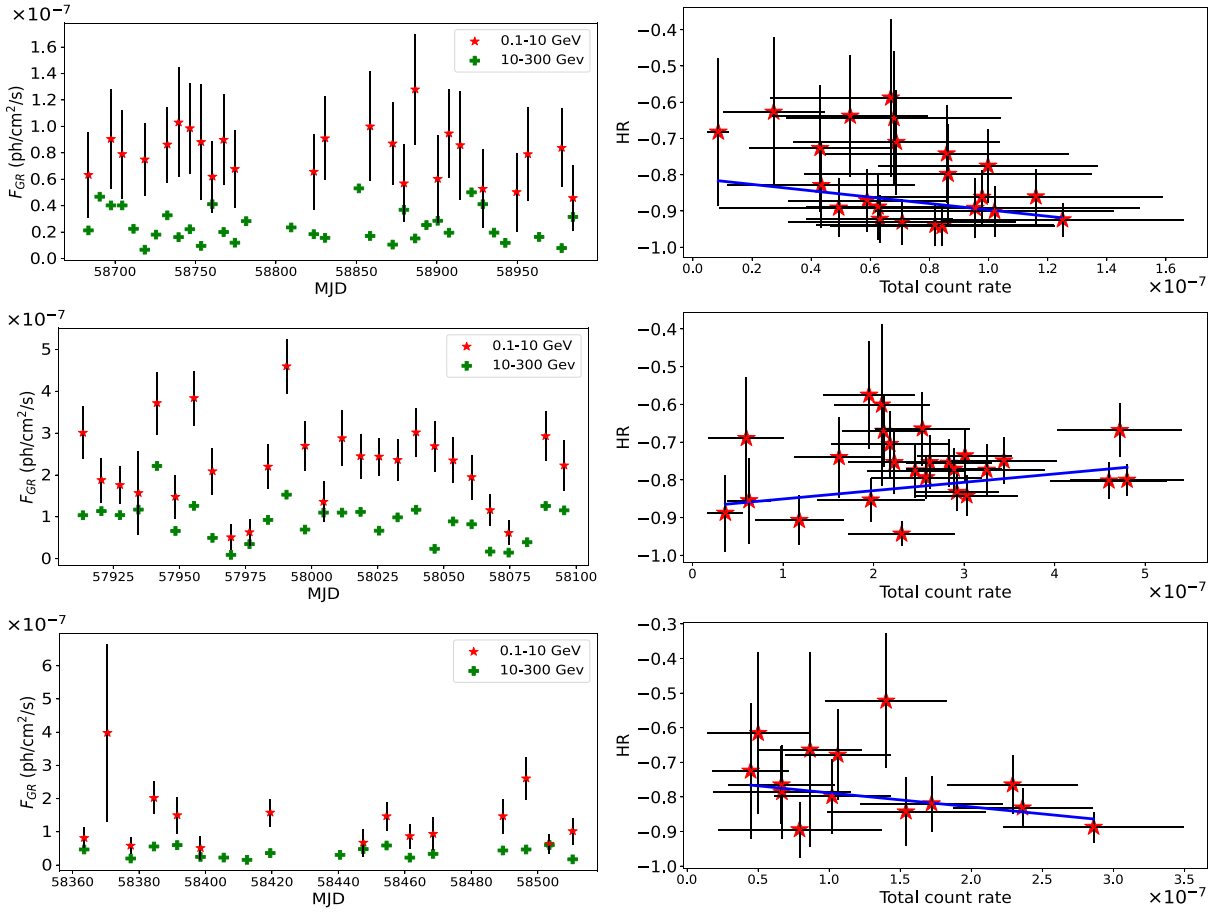

Figure 3. Left panels: 1 week binned γ-ray light curves for the epochs E_1 (top plot), E_2 (middle plot), and E_3 (bottom plot) in the 0.1−10 GeV (red) and 10−300 GeV multiplied by a factor of 5 (green) for TXS 0506+056. Right panels: the HR versus total intensity in the 0.1−300 GeV band for the epochs E_1 (top plot), E_2 (middle plot), and E_3 (bottom plot). The solid blue lines are the weighted linear least squares fit to the data.

For spectral fitting in XSPEC, we applied an absorbed *power-law* model, incorporating Galactic neutral hydrogen column densities of 7.33×10^{20} cm^{-2} for PKS 1424−418, 2.03×10^{20} cm^{-2} for PKS 1502+106, 1.22×10^{21} cm^{-2} for PKS 0446+112, and 1.15×10^{21} cm^{-2} for TXS 0506+056 (HI4PI Collaboration 2016).

2.3 UV and optical

For the analysis of UV and optical data covering the entire observation period, we utilized measurements from the *Swift* Ultraviolet/Optical Telescope (UVOT; P. W. A. Roming et al. 2005), a key instrument onboard the *Swift* spacecraft (N. Gehrels et al. 2004). The UVOT observations were performed using a combination of the *V*, *U*, UVW1, and UVW2 filters, which have central wavelengths (full width at half-maximum) values of 5468 Å (796 Å), 3465 Å (785 Å), 2600 Å (693 Å), and 1928 Å (657 Å), respectively (T. S. Poole et al. 2008). We processed the UVOT data using the online tools available in the *Swift* data archive, which automatically handles aspects such as data calibration and extraction of photometric measurements. To ensure an accurate representation of the intrinsic emission from the sources, we applied corrections for Galactic extinction to the observed UV and optical fluxes using the corresponding extinction values for each ROI (E. F. Schlafly & D. P. Finkbeiner 2011).

3 ANALYSIS AND RESULTS

3.1 Multiwavelength light curve

The multiwavelength light curves, which span 14 to 16 yr and cover γ-ray, X-ray, UV, and optical data from 2008 August to 2022 February/2024 May (MJD: 54500–59700/60460), are shown in Fig. 1 for the sources PKS 0446+112 and TXS 0506+056 and in Fig. 2 for the sources PKS 1424−418 and PKS 1502+106. From Figs 1 and 2 it is evident that all the sources showed both low and active states during the period analysed in this work. For each of the sources, we identified three epochs, denoted as E_1 (quiescent epoch), E_2 (epoch of neutrino detection), and E_3 (flaring epoch) for further analysis. Our definition of quiescent and flaring states in our sample of sources was primarily driven by the availability of near simultaneous multiband data across wavelengths needed for multiband SED modelling. They were identified from visual inspection of the long term γ-ray light curves. The details of these epochs, such as the start time, the end time, and the duration, are given in Table 2.

The selection of these epochs provides a detailed framework for investigating the spectral and temporal behaviour of these sources during the epoch of neutrino detection relative to other epochs. The source PKS 0446+112 was in the quiescent state in the γ-ray band most of the time of *Fermi* observations, except that it was in a flaring state on two epochs, one at ∼MJD 55 250 and the

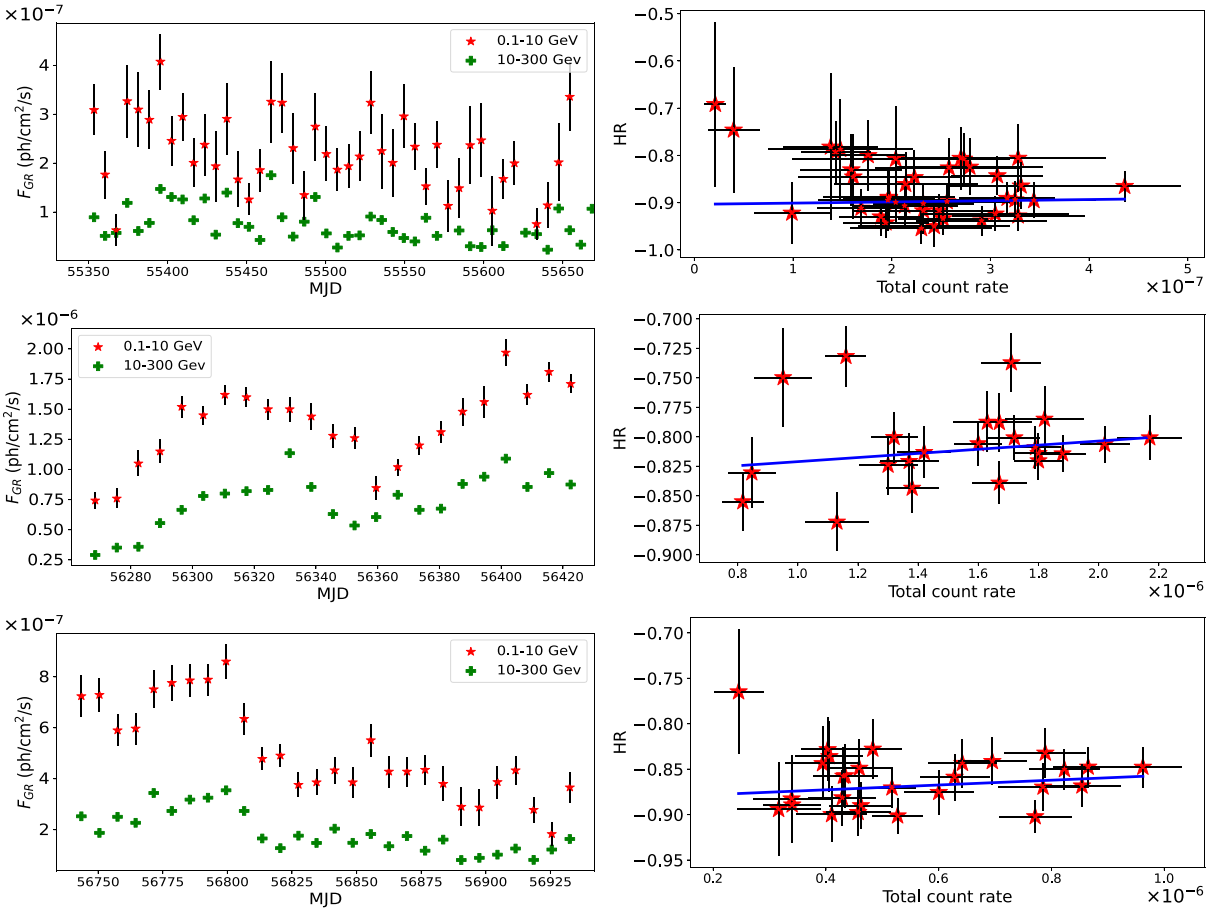

Figure 4. Left panels: 1 week binned γ-ray light curves for the epochs E_1 (top plot), E_2 (middle plot), and E_3 (bottom plot) in the 0.1−10 GeV (red) and 10−300 GeV multiplied by a factor of 3 (green) for PKS 1424−418. Right panels: the HR versus total intensity in the 0.1−300 GeV band for the epochs E_1 (top plot), E_2 (middle plot), and E_3 (bottom plot). The solid blue lines are the weighted linear least squares fit to the data.

other at ∼MJD 606265. Notably, it was in its brightest γ-ray activity state, at the epoch of neutrino emission. Similarly, a correlation between γ-ray flaring and neutrino activity was observed for TXS 0506+056 and PKS 1424−418 similar to that found in PKS 0735+178 (A. M. Bharathan et al. 2024b). PKS 1502+106 was in a low γ-ray activity state during the epoch of neutrino detection (see Fig. 2). Thus, we found no temporal correlation between γ-ray flaring activity and neutrino detection in PKS 1502+106. This was also reported by E. Kun et al. (2021), who noticed that while the source was in a low γ-ray activity state during the high-energy neutrino detection, the radio emission from PKS 1502+106 was in a high state at the epoch of neutrino detection. Varied correlation between the time period of neutrino detection and γ-ray flaring activity is also seen in the first neutrino blazar TXS 0506+056. While the γ-ray flaring activity in TXS 0506+056 during 2017 was found to have a temporal coincidence with the arrival of a 290 TeV neutrino event IC-170922A (IceCube Collaboration 2018b), the neutrino detection during 2014/15 (IceCube Collaboration 2018a) was not accompanied with an increased γ-ray activity (A. Franckowiak et al. 2020).

3.2 Variability analysis

3.2.1 Long-term variability

Long-term variability, spanning weeks to years, offers valuable insights into the processes governing the dynamics of the jet. To investigate the long-term variability of the sources during the epochs identified in Table 2, we estimated the fractional variability amplitude in the weekly binned light curves. Following S. Vaughan et al. (2003) we calculated the fractional variability, F_{var}, defined as

$$F_{var} = \sqrt{\frac{S^2 - \overline{\sigma_{err}^2}}{\bar{x}^2}} \tag{1}$$

In this equation, S^2 represents the variance of the flux over the selected period, $\bar{x}$ is the mean flux over the selected period, and $\overline{\sigma_{err}^2}$ is the mean square of the measurement errors associated with the flux points. We calculated the uncertainty in the fractional variability, $F_{var,err}$, following S. Vaughan et al. (2003) as

$$F_{var,err} = \sqrt{\frac{1}{2N}\left(\frac{\overline{\sigma_{err}^2}}{F_{var}\bar{x}^2}\right)^2 + \frac{1}{N}\frac{\overline{\sigma_{err}^2}}{\bar{x}^2}} \tag{2}$$

Here, N denotes the number of flux points in the light curve. By applying this method, we calculated γ-ray variability for all the selected epochs in each of the sources analysed in this work. The results of this variability analysis are presented in Table 3.

3.2.2 Short-term variability

Blazars are known to show flux variations on time-scales shorter than an hour (L. Foschini et al. 2011; S. Saito et al. 2013; A. Pandey

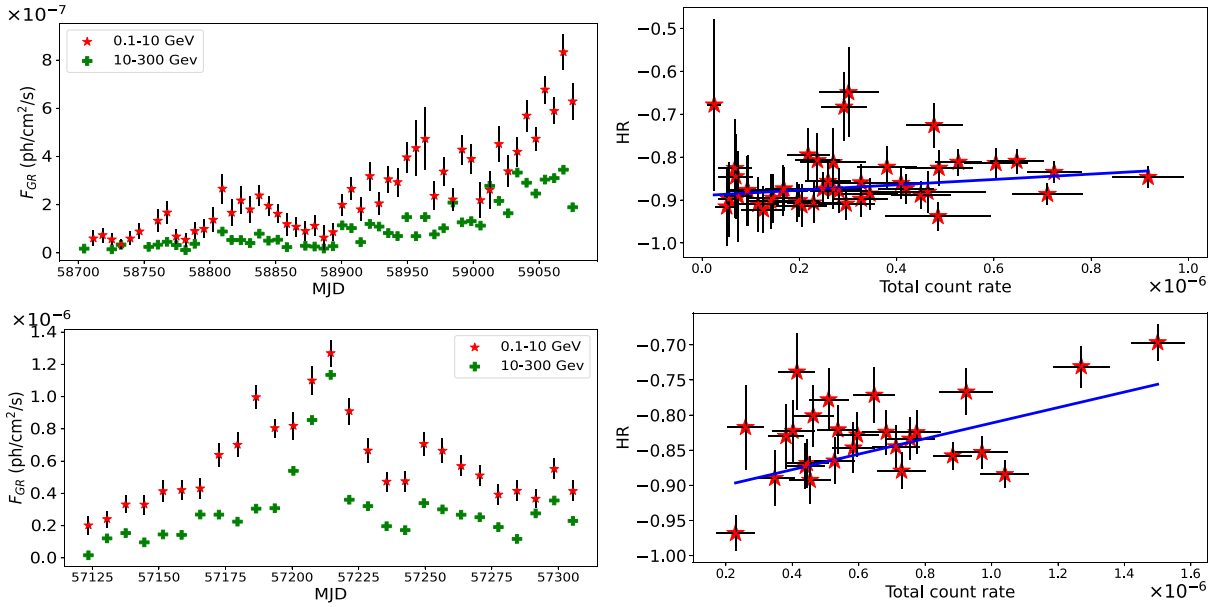

Figure 5. Left panels: 1 week binned γ-ray light curves for the epochs E_2 (top plot) and E_3 (bottom plot) in the 0.1−10 GeV (red) and 10−300 GeV multiplied by a factor of 3 (green) for PKS 1502+106. Right panels: the HR versus total intensity in the 0.1−300 GeV band for the epochs E_2 (top plot) and E_3 (bottom plot). The solid blue lines are the weighted linear least squares fit to the data.

Table 5. Results of the weighted linear least squares fit to the HR versus total intensity diagram. Here, R is the linear correlation coefficient and p is the probability for no correlation.

Source	Epochs	Slope	Intercept	R	p
TXS 0506+056	E_1	−879 573	−0.809	−0.482	0.019
	E_2	220 934	−0.873	0.124	0.546
	E_3	−405 588	−0.748	−0.388	0.170
PKS 1424−418	E_1	25 209	−0.903	−0.403	0.008
	E_2	17 464	−0.839	0.154	0.480
	E_3	26 468	−0.883	−0.008	0.969
PKS 1502+106	E_2	62 605	−0.889	0.133	0.381
	E_3	110 454	−0.922	0.492	0.009

& C. S. Stalin 2022). Detection of such short time-scale variation could enable one to constrain the size and the location of the γ-ray emission region. We therefore searched for the presence of flux variations on very short time-scales (of the order of hours) in the γ-ray light curves of PKS 0446+112, TXS 0506+056, PKS 1424−418, and PKS 1502+106 during their brightest γ-ray flaring epoch. For that, we calculated the flux doubling/halving time-scale using the following relation (A. M. Brown 2013):

$$F(t) = F(t_0) \times 2^{-(t-t_0)/\tau} \quad (3)$$

Here, F(t) and F(t_0) are the fluxes at times t and t_0, respectively, and τ is the flux doubling/halving time-scale. This calculation was done with the condition that the flux difference between epochs t and t_0 is greater than 2σ (L. Foschini et al. 2011). Using the flux doubling time-scale, we estimated the size of the γ-ray-emitting region as

$$r \leq c\tau\delta/(1+z), \quad (4)$$

where δ is the Doppler factor, τ is the flux doubling/halving time-scale, and c is the speed of light. The results of the analysis are given in Table 4. The flux doubling/halving time-scale is found to be in hours for BL Lacs and in few days for FSRQs, and the size of the γ-ray emission region is found to be in the range (3.7−74.7) $\times$ 10^{15} cm. These values are thus within the range of 1.68×10^{14} to 6.61×10^{19} cm found by J. Fan et al. (2023) based on an analysis of 2708 *Fermi* blazars.

3.2.3 *Spectral variability*

To examine the spectral variation in the sources during the selected epochs, we employed a model-independent method of calculating the hardness ratio (HR) and analysed its dependence on the source's total flux. For this purpose, we generated weekly binned γ-ray light curves in two energy ranges, 0.1−10 GeV and 10−300 GeV. We then calculated the HR and the associated error as (Y. K. Jin, S. N. Zhang & J. F. Wu 2008)

$$HR = \left(\frac{H-S}{H+S}\right) \quad (5)$$

$$\sigma_{HR} = \frac{2}{(H+S)^2}\sqrt{H^2\sigma_S^2 + S^2\sigma_H^2} \quad (6)$$

The light curves in the two energy ranges and the corresponding variation of HR with brightness of the sources for the selected epochs, where HR could be evaluated, are shown in Fig. 3 for TXS 0506+056, Fig. 4 for PKS 1424−418, and Fig. 5 for PKS 1502+106. We also carried out a weighted linear least squares fit to the HR versus intensity in the 0.1 − 300 GeV band and the results of the fit are given in Table 5. For TXS 0506+056, the diagram during epoch E_1 shows a possible softer-when-brighter behaviour. However, the scatter in the data points is relatively large, and during epochs E_2 and E_3 no clear correlation between HR and brightness is evident. For PKS 1424−418, the data in epoch E_1 suggest a harder-when-brighter trend, although the scatter prevents a firm conclusion. No clear trend is observed during epochs E_2 and E_3. For PKS 1502+106, the distribution during epoch E_3 indicates a possible harder-when-brighter behaviour, while during epoch E_2 no significant correlation is apparent.

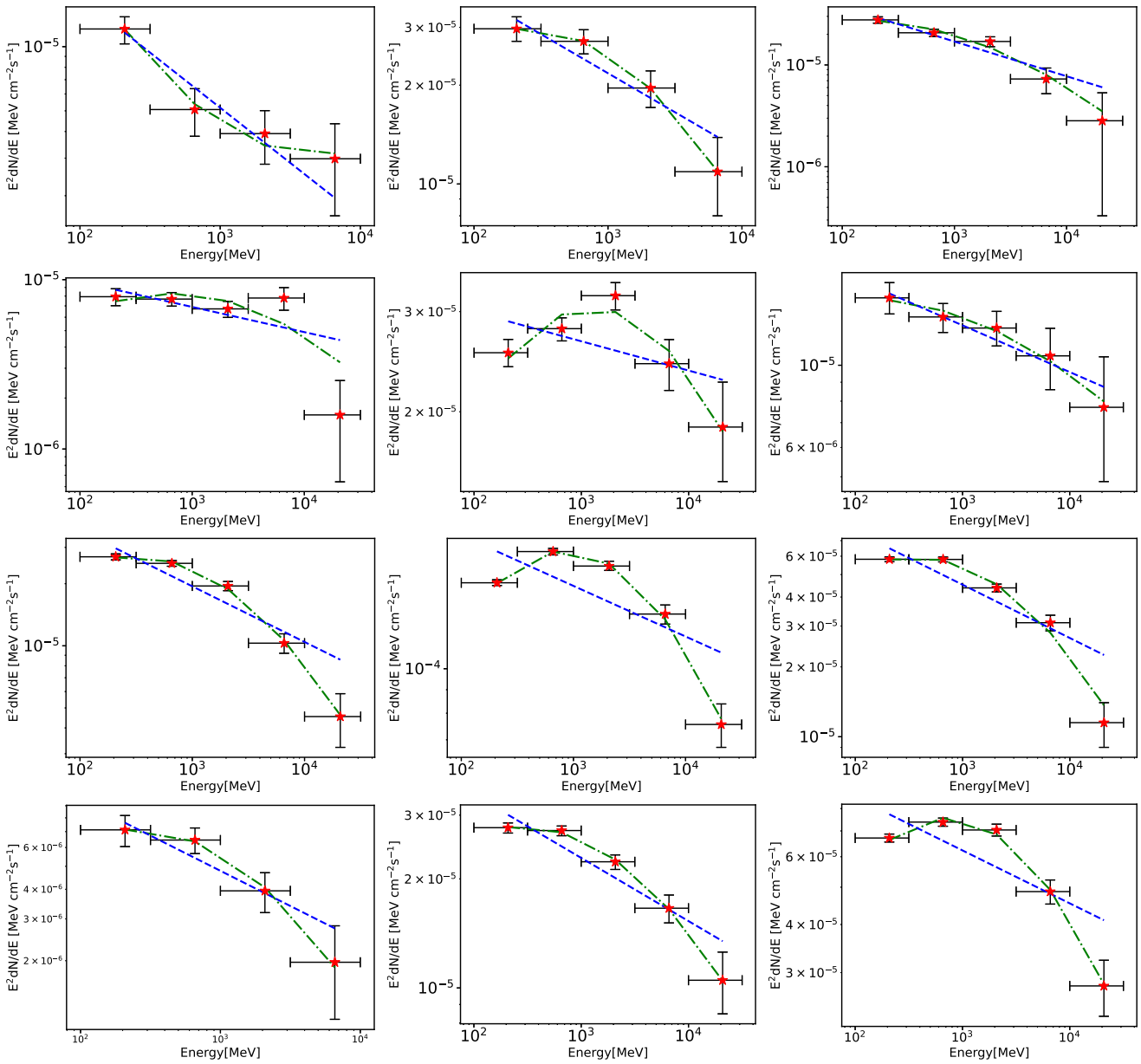

Figure 6. Simple power law (blue line) and log parabola (green line) fits to the γ-ray spectra of the sources analysed in this work during the epochs E_1 (left), E_2 (middle), and E_3 (right). For the top panels to the bottom panels, the sources are PKS 0446+112, TXS 0506+056, PKS 1424−418, and PKS 1502+106.

3.3 γ-ray spectra

Analysis of the γ-ray spectra can provide insights into the mechanisms responsible for high-energy emission. We analysed the γ-ray spectra for all the selected epochs in the sources using two spectral models namely the *power law* (PL) and *log parabola* (LP) models. The PL model has the functional form

$$\frac{dN(E)}{dE} = N_0 E^{-\Gamma} \tag{7}$$

Here, $\frac{dN(E)}{dE}$ is the differential photon number (cm^{-2} s^{-1} MeV^{-1}), N_0 is the normalization and Γ is the photon index.

The LP model has the functional form (P. L. Nolan et al. 2012),

$$\frac{dN(E)}{dE} = N_\circ (E/E_\circ)^{-\alpha-\beta ln(E/E_\circ)}, \tag{8}$$

where α is photon index at $E_\circ$, β defines the peak spectral curvature in the spectra, and $N_\circ$ and $E_\circ$ are the normalization and scaling factor of the energy spectrum, respectively.

We used the maximum likelihood estimator *gtlike* for the spectral analysis likelihood ratio test (J. R. Mattox et al. 1996) to check the PL model (null hypothesis) against the LP model (alternative hypothesis). We calculated the $TS_{curve} = 2(\log L_{LP} - \log L_{PL})$ following P. L. Nolan et al. (2012). We tested the presence of a significant curvature by setting the condition $TS_{curve} > 16$. The γ-ray spectra along with the model fits for the epochs E_1, E_2, and E_3 for the sources PKS 0446+112, TXS 0506+056, PKS 1424−418, and PKS 1502+016 are shown in Fig. 6. The parameters obtained for both PL and LP model fits are given in Table 6. The γ-ray spectra for all three epochs of PKS 0446+112 were well fit with a PL model. In the case of TXS 0506+056, epochs E_1 and E_2 were fit

Table 6. Results of the PL and LP model fits to the selected epochs of the four sources. Here, Γ is the photon index, Flux is the γ-ray flux value, TS is the test statistics, α is the spectral index, β is the measure of curvature in the spectra, and TS_{curve} signifies the presence of curvature in the spectra.

Source	Epochs	PL				LP				
		Γ	Flux	TS	L_{PL}	α	β	Flux	TS	L_{LP}	TS_{curve}
PKS 0446+112	E_1	−2.56	2.9×10^{-11}	102.7	−32 727.4	2.55 ±0.13	0.01 ± 0.00	3.1×10^{-11}	104.0	−32 730.4	−6
	E_2	−2.31	1.1×10^{-10}	592.9	−28 125.6	2.16 ±0.07	0.17 ± 0.04	1.2×10^{-10}	604.6	−28 118.8	13.6
	E_3	−2.33	8.9×10^{-11}	721.5	−35 483.8	2.22 ±0.07	0.11 ± 0.04	5.2×10^{-12}	728.5	−35 480.6	7.6
TXS 0506+056	E_1	−2.16	9.9×10^{-12}	864.9	−36 394.3	2.14± 0.05	$3.7\times10^{-4}\pm2.5\times10^{-5}$	9.8×10^{-12}	837.4	−36 394.8	−0.8
	E_2	−2.12	5.6×10^{-12}	836.5	−56 832.2	2.09± 0.06	0.06 ± 0.03	6.1×10^{-12}	830.7	−56 834.1	3.8
	E_3	−2.0	2.2×10^{-11}	3635.1	−48 360.6	1.99± 0.03	0.07 ± 0.02	2.4×10^{-11}	3629.2	−48 348.7	23.8
PKS 1424−418	E_1	−2.25	4.6×10^{-11}	4513.2	−81 341.7	2.21 ± 0.02	0.11 ± 0.02	5.5×10^{-11}	4704.5	−81 298.6	86.2
	E_2	−1.86	1.0×10^{-10}	23 884.6	−54 766.7	1.99 ± 0.01	0.09 ± 0.01	3.9×10^{-10}	31 919.6	−53 817.0	1899.4
	E_3	−2.21	9.9×10^{-11}	10 111.1	−67 345.2	2.16 ±0.02	0.09 ± 0.01	1.2×10^{-10}	10 314.7	−67 299.3	91.8
PKS 1502+106	E_1	−2.06	1.0×10^{-11}	201.5	−28 964.8	2.38 ±0.09	0.02 ± 0.01	2.4×10^{-11}	698.6	−29 004.9	238.8
	E_2	−1.37	1.0×10^{-11}	3550.5	−56 113.1	2.07 ±0.03	0.08 ± 0.01	1.1×10^{-10}	6629.5	−55 081.3	2063.6
	E_3	−1.09	1.0×10^{-11}	5274.9	−42 376.6	1.96 ±0.02	0.09 ± 0.02	3.1×10^{-10}	13 108.4	−39 469.9	5813.4

with a PL model, while epoch E_3 required the LP model. For PKS 1424−418 and PKS 1502+106, all the epochs were well described by a LP model.

3.4 Broad-band SED analysis

3.4.1 One-zone leptonic modelling

We also carried out broad-band SED analysis of all the three epochs for each of the sources. For this we used the one-zone leptonic framework described in S. Sahayanathan & S. Godambe (2012). This model assumes the emission to originate from a spherical region of radius R, moving down the jet relativistically with Lorentz factor (Γ) and filled with a tangled magnetic field. The jet is inclined at an angle θ with the line of sight and hence the observed emission will be boosted by the Doppler factor δ. The emission region is filled with a non-thermal electron distribution following a broken power law with indices p and q, described as

$$N(\gamma)\,\mathrm{d}\gamma = \begin{cases} K\,\gamma^{-p}\,\mathrm{d}\gamma & \text{for} \quad \gamma_{\min} < \gamma < \gamma_b \\ K\,\gamma_b^{q-p}\gamma^{-q}\,d\gamma & \text{for} \quad \gamma_b < \gamma < \gamma_{\max} \end{cases}, \tag{9}$$

where γ is the electron Lorentz factor and γ_b corresponds to the break Lorentz factor. The electrons radiate via synchrotron emission and inverse Compton scattering through either SSC or EC processes. We assumed the emission region to be beyond the BLR but within the IR torus. Hence, due to relativistic boosting the dominant photon fields will be the IR dust emission which is chosen as a blackbody at 1000 K. The emissivity due to these emission processes was computed numerically under steady-state, and the flux received on Earth is used to reproduce the observed spectrum. The best-fitting SEDs using this model for PKS 0446+112, TXS 0506+056, PKS 1424−418, and PKS 1502+106 are shown in Figs 7, 8, 9, and 10, respectively. The results of the SED analysis are given in Table 7.

3.4.2 Hadronic SED modelling

For the epochs in which the simple one-zone leptonic model failed to reproduce the observed high-energy emission (epoch E_2 of PKS 0446+112 and epoch E_2 of PKS 1502+106), we employed the stationary hadronic model described in M. Böttcher et al. (2013). The model assumes a spherical emission region of radius R, moving relativistically with bulk Lorentz factor Γ and Doppler factor δ, and permeated by a tangled magnetic field B, similar to the leptonic framework.

In addition to a non-thermal electron population, the emission region contains relativistic protons injected with a power-law energy distribution between $\gamma_{p,\min}$ and $\gamma_{p,\max}$. Particle escape is parametrized by an escape time-scale $t_{\rm esc} = \eta_{\rm esc}R/c$, while the particle distributions are evolved under steady-state conditions accounting for radiative particle cooling and interactions.

The relativistic electrons radiate through SSC processes, while the high-energy component is dominated by proton synchrotron radiation and photohadronic ($p\gamma$) interactions. The proton synchrotron emission is calculated using the standard synchrotron formalism,

$$P_{\rm syn}(\nu) \propto \int N_p(\gamma_p) F\left(\frac{\nu}{\nu_c(\gamma_p)}\right) \mathrm{d}\gamma_p, \tag{10}$$

where $N_p(\gamma_p)$ is the proton energy distribution and $\nu_c(\gamma_p) = \frac{3eB}{4\pi m_p c}\gamma_p^2$ is the critical proton synchrotron frequency. The $p\gamma$ interactions are treated using the semi-analytical approach of M.

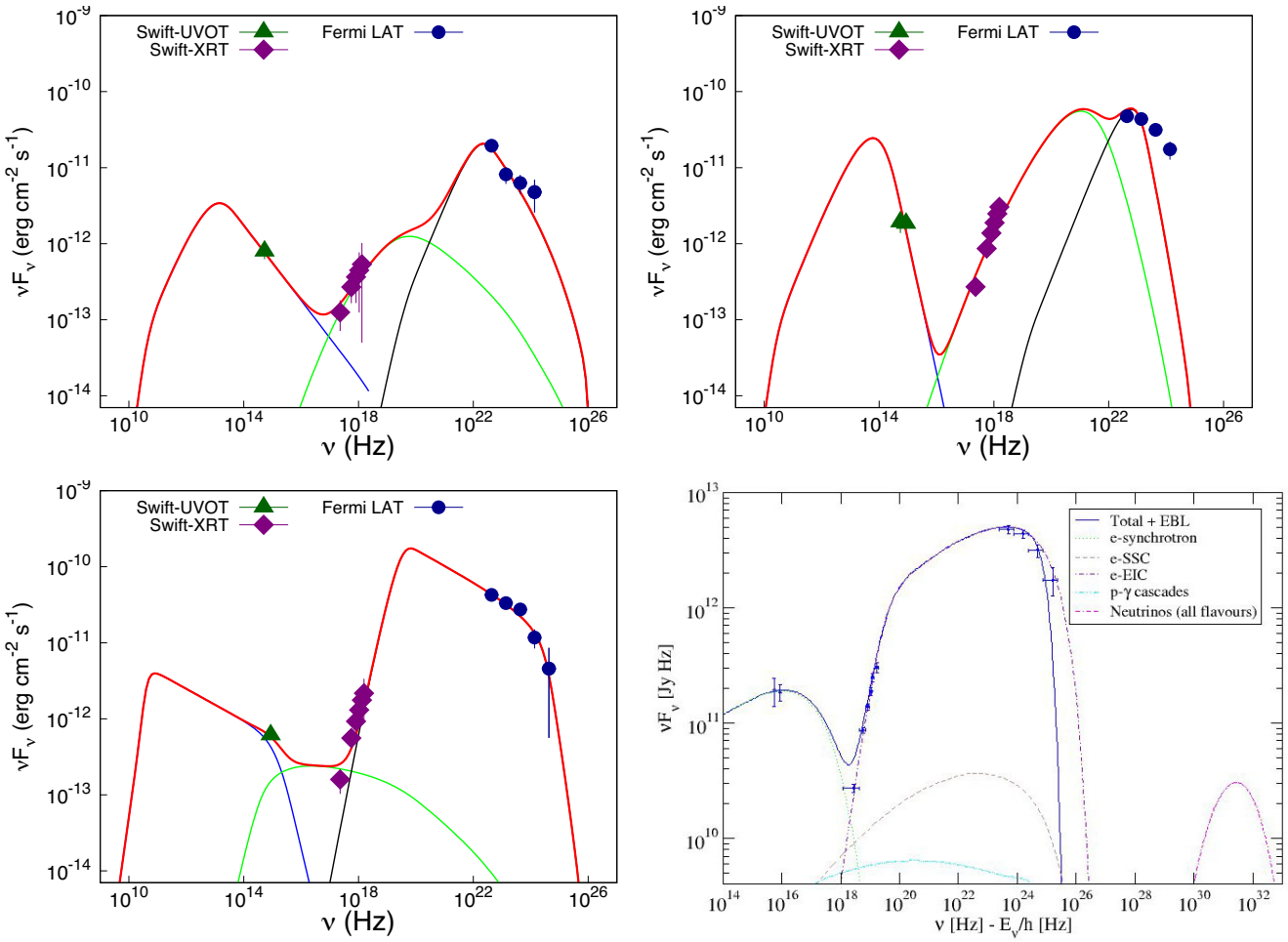

Figure 7. Broad-band SEDs along with the one zone leptonic emission model fits for the epochs E_1 (top left panel), E_2 (top right panel), and E_3 (bottom left panel) of PKS 0446+112. In all the fits, the blue line refers to the synchrotron model, the green line refers to the SSC process, and the black line refers to the EC process. The red line is the sum of all the three components. The bottom-right panel shows the hadronic fit to the SED of the epoch E_2.

Böttcher et al. (2013), based on the templates of S. R. Kelner & F. A. Aharonian (2008), which provide the spectra of secondary photons, neutrinos, and electron–positron pairs. The model self-consistently accounts for secondary emission processes, including photons from π^0 decay, synchrotron radiation from secondary $e^{\pm}$ produced in charged pion and muon decays, and synchrotron-supported pair cascades initiated by internal $\gamma\gamma$ absorption. This framework was applied to epoch E_2 of PKS 0446+112 and PKS 1502+106, where the purely leptonic model could not adequately reproduce the observed γ-ray flux. The resulting best-fitting SEDs are shown in Figs 7 and 10, and the corresponding parameters are listed in Table 8.

For PKS 0446+112, the hadronic modelling yields results that are qualitatively consistent with the findings of R. Khatoon, M. Boettcher & J. Robinson (2025). The very hard X-ray spectrum strongly constrains the possible contribution from hadronic processes, effectively ruling out a dominant proton-synchrotron component in the observed SED. Instead, the broad-band emission is primarily electron-dominated, with only a subdominant hadronic contribution at the highest energies. The derived model parameters exhibit near-equipartition between particle and magnetic energy densities, with $L_B/L_e \sim 1$, indicating a physically well-balanced jet configuration.

The predicted neutrino flux from photohadronic interactions is found to be very low, consistent with the absence of a significant excess reported by the IceCube Neutrino Observatory apart from the single neutrino alert. Overall, while a lepto-hadronic scenario can reproduce the observed SED, the hard X-ray spectrum implies that the emission is predominantly leptonic in nature during this epoch.

For PKS 1502+106, a satisfactory reproduction of the high-energy component required a hybrid scenario in which the low- and intermediate-energy emission is dominated by synchrotron and SSC processes, while the γ-ray emission is primarily contributed by hadronic interactions. Although this configuration provides a reasonable fit to the observed SED, the derived physical parameters are rather extreme. In particular, the required proton kinetic power is highly super-Eddington, and the electron energy distribution is characterized by a very hard spectral index (~ 5), which is uncommon in standard shock-acceleration scenarios. These factors suggest that, while the lepto-hadronic model can formally reproduce the observed spectrum, the required physical

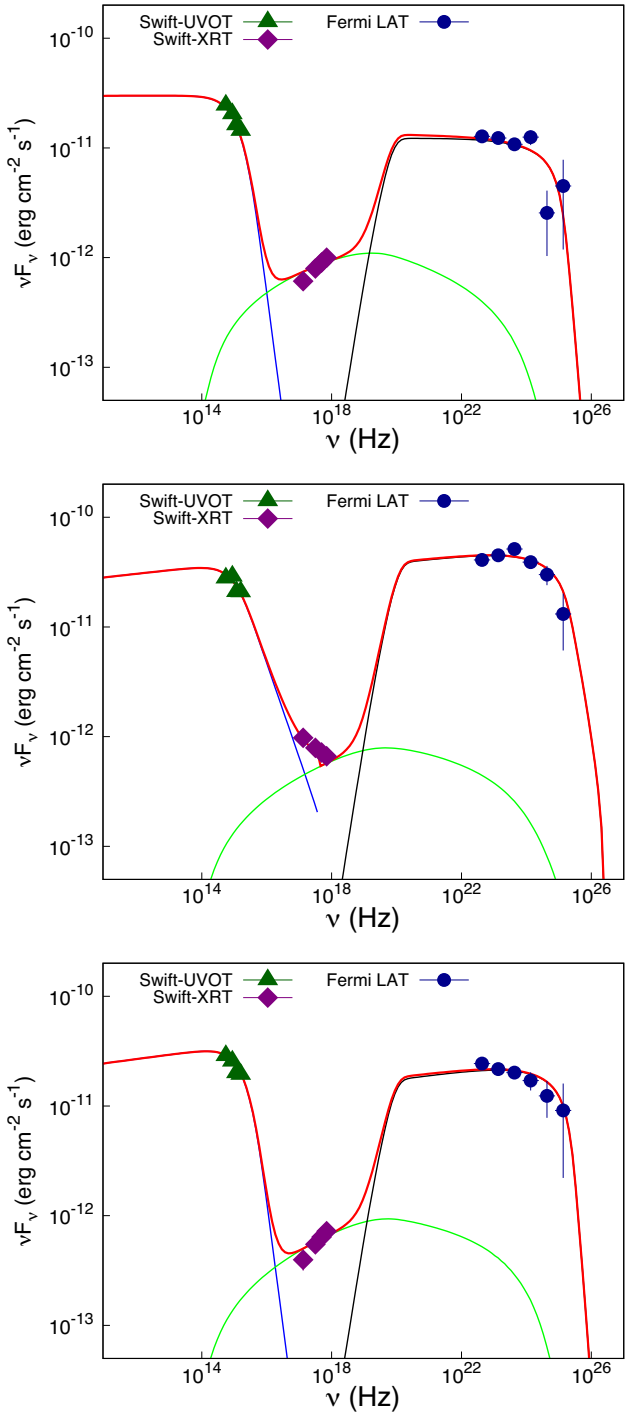

Figure 8. Broad-band SEDs along with the one zone leptonic emission model fits for the epochs E_1 (top panel), E_2 (middle panel), and E_3 (bottom panel) of TXS 056+056. In all the fits, the blue line refers to the synchrotron model, the green line refers to the SSC process, and the black line refers to the EC process. The red line is the sum of all the three components.

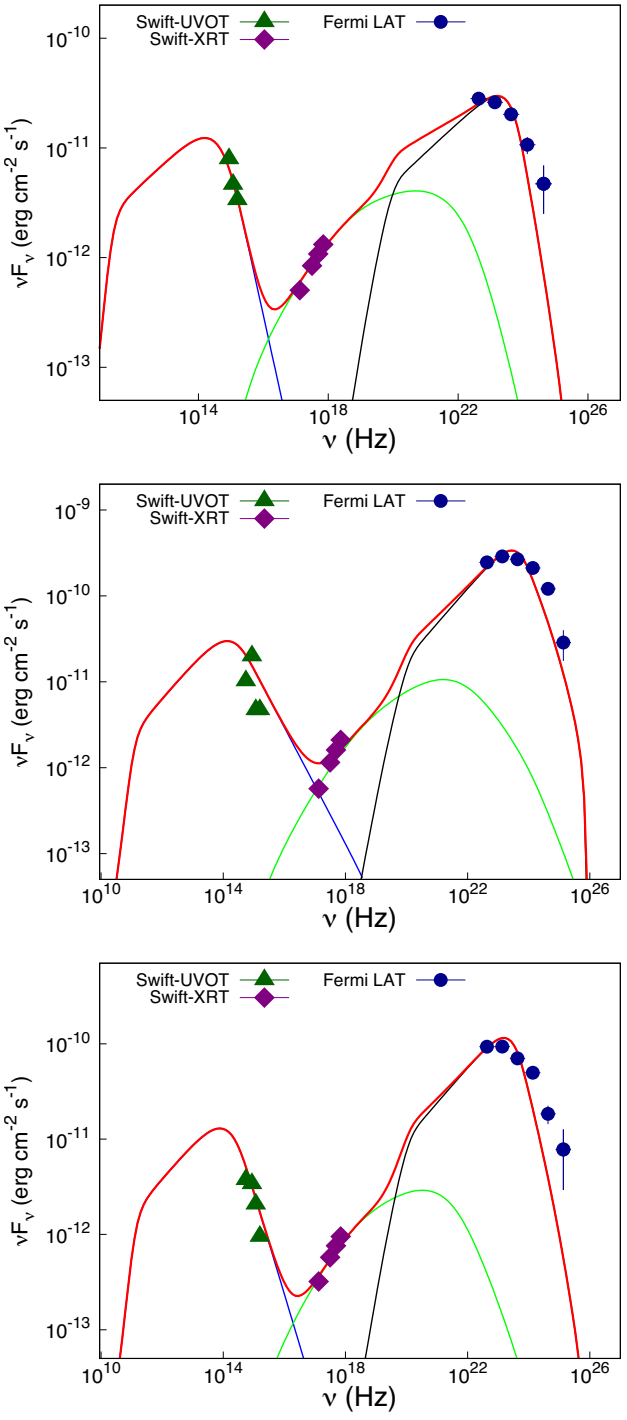

Figure 9. Broad-band SEDs along with the one zone leptonic emission model fits for the epochs E_1 (top panel), E_2 (middle panel), and E_3 (bottom panel) of PKS 1424−418. In all the fits, the blue line refers to the synchrotron model, the green line refers to the SSC process, and the black line refers to the EC process. The red line is the sum of all the three components.

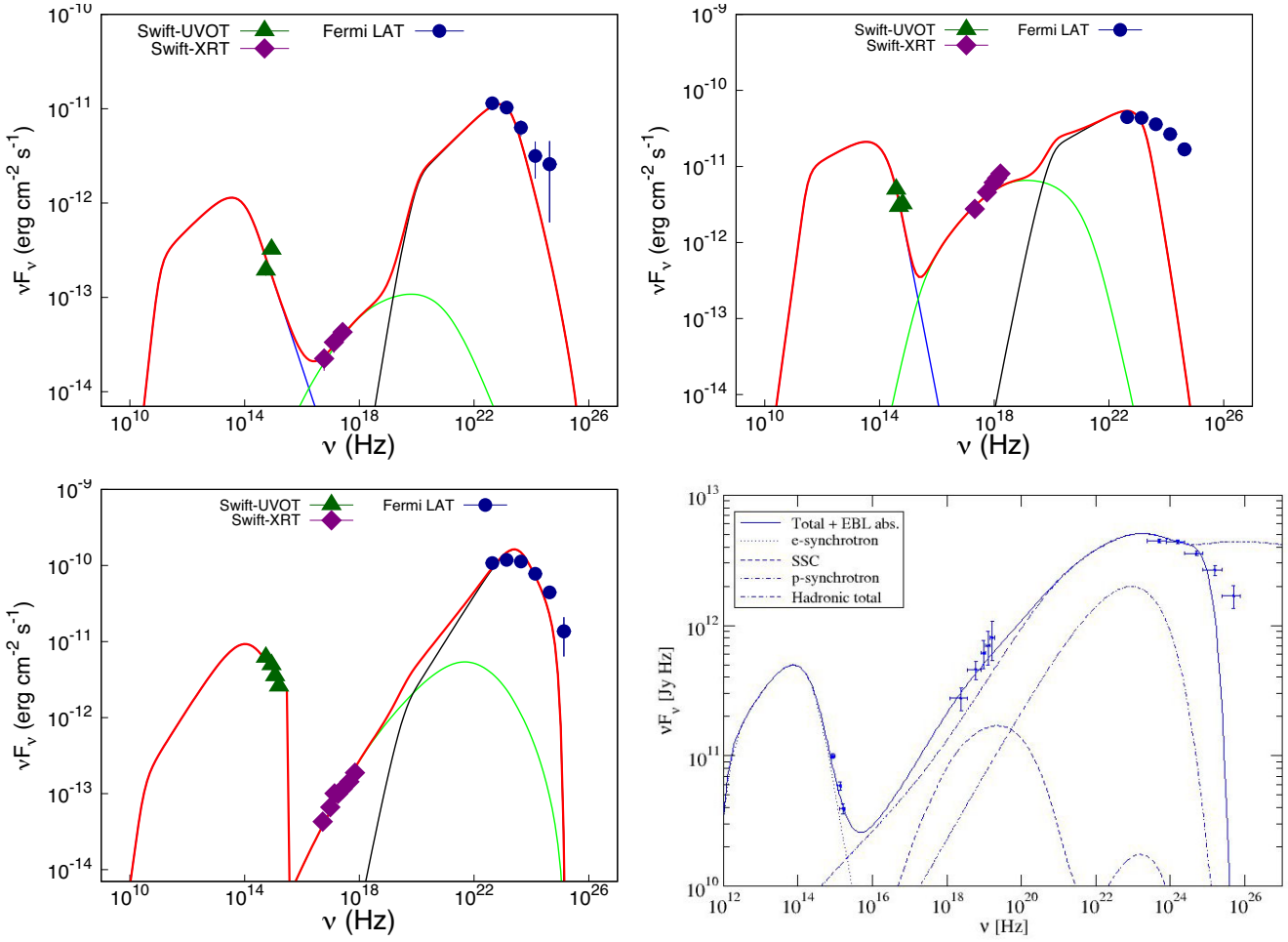

Figure 10. Broad-band SEDs along with the one zone leptonic emission model fits for the epochs E_1 (top left panel), E_2 (top right panel), and E_3 (bottom left panel) of PKS 1502+106. In all the fits, the blue line refers to the synchrotron model, the green line refers to the SSC process, and the black line refers to the EC process. The red line is the sum of all the three components. The bottom-right panel shows the hadronic fit to the SED of the epoch E_2.

Table 7. Results of the broad-band SED analysis carried out for the selected epochs of PKS 1424−418, PKS 1502+106, PKS 0446+112, and TXS 0506+056. The parameters p and q are the low- and high-energy power-law indices of the electron distribution, γ_b is the the break energy, R is the size of the emission blob in cm, Γ is the bulk Lorentz factor, and B is the magnetic field in Gauss. In our modelling, we considered a minimum electron Lorentz factor of $\gamma_{\rm min,e} = 50$ and a maximum of $\gamma_{\rm max,e} = 9.5 \times 10^5$.

Source	Epoch	p	q	γ_b	log (R) (cm)	Γ	B (G)
PKS 0446+112	E_1	1.16	3.99	1156.3	16.99	12.54	0.34
	E_2	1.1	6.49	3890.6	17.42	50	0.34
	E_3	3.42	6.18	18 331	18.09	11.97	0.12
TXS 0506+056	E_1	3.0	7.5	25 867	18.49	9.02	0.03
	E_2	2.93	4.7	26 153	18.6	11.91	0.02
	E_3	2.92	7.5	33 971.5	18.54	10.05	0.02
PKS 1424−418	E_1	2.29	6.84	3874.6	16.68	50	0.68
	E_2	2.17	4.36	3681.2	17.07	28.61	0.32
	E_3	2.25	5.13	2933.6	16.92	28.63	0.37
PKS 1502+106	E_1	2.38	4.84	2215.2	16.72	28.9	0.36
	E_2	2.57	6.9	2000	16.81	29.6	0.70
	E_3	1.77	7.00	4702.78	16.88	29.63	0.35

Table 8. Results of hadronic model fits to epoch E_2 for PKS 0446+11 and PKS 1502+106.

Parameter	PKS 0446+11	PKS 1502+106
Minimum Lorentz factor ($\gamma_{\rm min}$)	50	7×10^2
Maximum Lorentz factor ($\gamma_{\rm max}$)	5×10^4	1×10^4
Electron spectral index (α_e)	1.7	5.0
Magnetic field (B [G])	1.1	3
Blob radius (R [cm])	3×10^{16}	3.5×10^{15}
Bulk Lorentz factor (Γ)	20	35
Observing angle ($\theta_{\rm obs}$ [°])	1	1
Accretion disc luminosity (L)	1×10^{46}	1×10^{46}
Black hole mass [$M_\odot$]	5×10^8	5×10^8
$E_{p,\rm min}$ [GeV]	1	1
$E_{p,\rm max}$ [GeV]	2.5×10^9	1×10^9
Proton spectral index (α_p)	1.9	2.0
IR temperature$T_{\rm ext}$ [K]	1×10^3	–
IR photon field$u_{\rm ext}$ [erg cm^{-3}]	1.5×10^{-3}	–
L_e [erg s^{-1}]	1.6×10^{45}	2.4×10^{44}
L_B [erg s^{-1}]	1.6×10^{45}	5.1×10^{44}
L_p [erg s^{-1}]	1.0×10^{45}	9.0×10^{49}
L_B/L_e	1.02	2.11
L_B/L_p	1.63	5.63×10^{-6}
L_e/L_p	1.60	2.67×10^{-6}

conditions may be challenging from an energetic and theoretical standpoint.

4 DISCUSSION AND SUMMARY

Blazars are now increasingly found to be associated with neutrinos detected by IceCube. These observations are therefore beginning to put constraints on the physical processes that happen in the relativistic jets of these sources. The neutrino detection along with simultaneous/near simultaneous follow-up observations over a range of wavelengths have now enabled better understanding of the broad-band SEDs of blazars, which also involves development of theories or models involving leptons, hadrons, and photons (S. Gasparyan, D. Bégué & N. Sahakyan 2022; S. I. Stathopoulos et al. 2024; N. Sahakyan et al. 2024a). These multimessenger observations will help in a better understanding of their relativistic jets. In this work, we carried out such a study on four neutrino blazars namely PKS 0446+112, TXS 0506+056, PKS 1424−418, and PKS 1502+106. The results are summarized below.

(i) Of the four sources studied in this work, we found a temporal correlation between neutrino detection and flaring γ-ray activity in three sources, namely, PKS 0446+112, TXS 0506+056, and PKS 1424−418. However, we found no temporal correlation between neutrino detection and γ-ray flaring activity in the source PKS 1502+106. Similarly, during the neutrino flare detected in the year 2014/15, in TXS 0506+056, no flaring activity in γ-rays was noticed (A. Franckowiak et al. 2020). Therefore, neutrino detection does not necessarily correspond to flaring γ-ray activity. These findings consistent with earlier results (F. Oikonomou et al. 2021; R. Abbasi et al. 2023) underscore the complexity of blazar emission processes and indicate that neutrino emission in blazars may not necessarily coincide with their flaring γ-ray activity states.

(ii) All the four sources are found to be variable in γ-rays. Concentrating on the brightest γ-ray activity of the sources (which also corresponds to the epoch of neutrino detection in PKS 0446+112, TXS 0506+056, and PKS 1424−418) we found flux doubling/halving time-scale of 4.70, 9.24, 30.76, and 15.42 h in the sources PKS 0446+112, TXS 0506+056, PKS 1424−418, and PKS 1502+106, respectively. From these observed flux doubling/halving time-scale, we found the size of the emission region as 3.70×10^{15} cm for PKS 0446+112, 7.47×10^{16} cm for TXS 0506+056, 2.63×10^{16} cm for PKS 1424−418, and 7.04×10^{15} cm for PKS 1502+106. These values are found to lie in the range mentioned by J. Fan et al. (2023) through an analysis of thousands of *Fermi* blazars. This points to a compact emission region within the relativistic jets of these sources. The difference in emission region sizes from rapid variability and SED modelling is expected. Variability traces compact sub-structures responsible for fast flares, while SED modelling reflects a larger averaged region producing the total flux. Thus, the two estimates probe different physical scales within the jet.

(iii) The location of the γ-ray-emitting region (relative to the central black hole) was estimated using the observed flux doubling/halving time-scales together with the bulk Lorentz factors derived from the SED modelling (F. Tavecchio et al. 2010).

$$r_{\rm em} \lesssim \frac{2c\Gamma^2\tau}{1+z} \tag{11}$$

We obtained distances of $r_{\rm em} \approx 8.1 \times 10^{17}$ cm for PKS 0446+112, 2.1×10^{17} cm for TXS 0506+056, 2.2×10^{18} cm for PKS 1424−418, and 1.0×10^{18} cm for PKS 1502+106. These values suggest that the location of the emission region is beyond the typical BLR radius (10^{16}-10^{17} cm; G. Ghisellini & P. Madau 1996), but within the dusty torus (10^{18}-10^{19} cm). Hence, the dominant EC emission mechanism will be the EC scattering of IR photons.

(iv) We also investigated the spectral variations of the sources in all epochs where both soft and hard γ-ray light curves could be generated. For PKS 1424−418 and PKS 1502+106, the diagrams suggest a tendency for spectral hardening with increasing total brightness, although the scatter in the data points prevents firm conclusions. For TXS 0506+056, the data indicate a possible softer-when-brighter behaviour.

(v) For all the sources, we investigated the nature of the γ-ray spectra in three epochs, one corresponding to the epoch of neutrino detection, the second one corresponding to a quiescent activity of the sources, and the third one corresponding to a flaring state of the sources. The spectra were well fit with a power law for the source PKS 0446+112. For the source TXS 0506+056, power-law model fits the spectra well during epochs E_1 and E_2, while during epoch E_3, log parabola model fits the spectrum well compared to the power-law model. For the sources PKS 1424−418 and PKS 1502+016 a log parabola model was found to well explain the spectra.

(vi) For the source PKS 1424−418, all three epochs analysed in this study are well modelled in the leptonic scenario. However, S. Gao, M. Pohl & W. Winter (2017), who investigated the source during different activity phases concluded that a lepto-hadronic model with a sub dominant hadronic component could explain its SED. A more recent investigation by X. Rodrigues et al. (2024) also found the SED of PKS 1424−418 to be compatible with a leptonic model in agreement with the results presented in this work.

(vii) For PKS 1502+106, the broad-band SEDs during both the quiescent state (Epoch E_1) and the flaring state (Epoch E_3) were successfully reproduced with a leptonic emission model incorporating synchrotron, SSC, and EC processes. However, during epoch E_2, which corresponds to the time of the neutrino detection

and a faint γ-ray flux state, an additional hadronic component was required to explain the broad-band emission (see bottom right panel of Fig. 10). Within the lepto-hadronic framework, the high-energy emission during this epoch is primarily attributed to proton synchrotron radiation and $p\gamma$ interactions. Although this scenario provides a satisfactory fit to the observed SED, it requires extreme physical conditions, including a highly super-Eddington proton kinetic power and an unusually hard electron energy distribution. These energetic requirements suggest that, while the hadronic contribution can account for the observed spectrum, the implied jet parameters are challenging from a physical standpoint.

The short variability time-scale and the probable detection of a neutrino during this epoch further support the presence of both leptonic and hadronic emission mechanisms. Modelling of the broad-band SED of PKS 1502+106 across three activity states, including the neutrino detection epoch, was previously carried out by X. Rodrigues et al. (2021). We note here that our identification of flaring and quiescent epochs was based on visual examination and the requirement of multiband data. In contrast, X. Rodrigues et al. (2021) identified flaring periods using Bayesian block analysis and defined the quiescent state based on flux measurements during a low-activity period. They found that hadronic models can account for the multiwavelength emission during all three states as well as the observed neutrino signal during its quiescent state. A similar scenario is observed in another neutrino source, PKS 0735+178, for which SED modelling indicates that the quiescent state required a photomeson process to explain the emission, whereas the flaring state, which coincided with the neutrino detection epoch, could be adequately explained by a one-zone leptonic model (A. Acharyya et al. 2023; N. Sahakyan et al. 2023; A. M. Bharathan et al. 2024b; R. Prince et al. 2024; A. Omeliukh et al. 2025).

(viii) For the source PKS 0446+112, while the SEDs of the quiescent and flaring episodes are well reproduced by purely leptonic processes, the epoch of neutrino detection (Epoch E_2) required an additional hadronic component to account for the observed high-energy emission. The very hard X-ray spectrum during this epoch strongly constrains the contribution from proton synchrotron radiation, implying that the emission remains largely electron-dominated with only a subdominant hadronic contribution. The derived model parameters are close to equipartition ($L_B/L_e \sim 1$), indicating a physically plausible jet configuration. The predicted neutrino flux in this scenario is very low, consistent with the absence of a significant excess reported by IceCube apart from the single neutrino alert.

(ix) For TXS 0506+056, all the three epochs analysed in this work including the one coinciding with the 2017 IceCube-170922A are well explained by a purely leptonic emission scenario. Previously, M. Petropoulou et al. (2020) modelled the broad-band SED of the source using contemporaneous data in optical, X-ray, and γ-ray energies across four epochs, including the period 2014–2015, during which a neutrino flare with a significance of 3.5σ was reported from the direction of TXS 0506+056 (IceCube Collaboration 2018a). They found the SEDs are consistent with a hybrid scenario, where the γ-rays are produced by EC processes and the observed neutrinos arise from photomeson processes of co-accelerated protons. The difference in the preferred emission scenarios across epochs, purely leptonic in some cases (this work), and hybrid leptonic process in other epochs (M. Petropoulou et al. 2020) may be due to (a) the varying dominance of leptonic and hadronic components at different epochs, (b) the emission originating from different regions during different epochs, and/or (c) complex physical processes not fully captured by current models.

This work underscores the importance of coordinated multi-wavelength and multimessenger observations to unravel the complexities of blazar jets. It is anticipated that more neutrino blazars will be detected in the future with the current as well as future neutrino experiments. As of now, we are aware of two sources, namely, TXS 0506+056 and PKS 1502+106, that were in a low γ-ray flux state at the time of IceCube neutrino detections. With an increasing number of detected neutrino blazars, it is likely that more sources exhibiting similar behaviour will be identified. Timing, spectral, and SED model fits to a large sample of neutrino blazars will further help to refine our understanding of the physical mechanisms of these enigmatic sources.

ACKNOWLEDGEMENTS

We thank the referee for constructive comments and suggestions that helped to improve the quality of this manuscript. AMB acknowledges the Department of Science and Technology (DST) for the INSPIRE Fellowship (IF200255). AMB also thanks the Center for Research, CHRIST (Deemed to be University) and Centre for Space research (CSR), North-West University for their support during the course of this work. This work makes use of archival γ-ray data from the Fermi Science Support Center (FSSC) and *Swift*-XRT/UVOT data from the High Energy Astrophysics Science Archive Research Center (HEASARC).

DATA AVAILABILITY

All the data used here for analysis is publicly available and the results are incorporated in the paper.

REFERENCES

Aartsen M. G. et al., 2014, Phys. Rev. Lett., 113, 101101
Aartsen M. G. et al., 2017, J. Instrum., 12, P03012
Aartsen M. G. et al., 2020, Phys. Rev. Lett., 124, 051103
Abbasi R. et al., 2023, ApJ, 954, 75
Abdo A. A. et al., 2010a, ApJ, 710, 810
Abdo A. A. et al., 2010b, ApJ, 716, 30
Abdollahi S. et al., 2020, ApJS, 247, 33
Abhir J., Joseph J., Patel S. R., Bose D., 2021, MNRAS, 501, 2504
Acharyya A. et al., 2023, ApJ, 954, 70
Angel J. R. P., Stockman H. S., 1980, ARA&A, 18, 321
Atwood W. B. et al., 2009, ApJ, 697, 1071
Begelman M. C., Sikora M., 1987, ApJ, 322, 650
Benke P. et al., 2024, A&A, 681, A69
Bharathan A. M., Stalin C. S., Chatterjee R., Sahayanathan S., Pal I., Mathew B., Agrawal V. K., 2024a, JA&A, 45, 35
Bharathan A. M., Stalin C. S., Sahayanathan S., Bhattacharyya S., Mathew B., 2024b, MNRAS, 529, 3503
Bharathan A. M. et al., 2024c, ApJ, 975, 185
Bhatta G., 2021, ApJ, 923, 7
Blandford R. D., Rees M. J., 1978, Phys. Scr, 17, 265
Błażejowski M., Sikora M., Moderski R., Madejski G. M., 2000, ApJ, 545, 107
Böttcher M., Reimer A., Sweeney K., Prakash A., 2013, ApJ, 768, 54
Brown A. M., 2013, MNRAS, 431, 824
Burrows D. N. et al., 2005, Space Sci. Rev., 120, 165
Buson S., Tramacere A., Pfeiffer L., Oswald L., de Menezes R., Azzollini A., Ajello M., 2022, ApJ, 934, L38
Buson S. et al., 2023, preprint (arXiv:2305.11263)

Butuzova M. S., Guseva V. A., Gorbachev M. A., Krivenko A. S., Nazarov S. V., 2025, J. High Energy Astrophys., 45, 19
Dermer C. D., Schlickeiser R., 1993, ApJ, 416, 458
Dermer C. D., Schlickeiser R., Mastichiadis A., 1992, A&A, 256, L27
de Jaeger T. et al., 2023, MNRAS, 519, 6349
Dominici T. P., Abraham Z., Teixeira R., Benevides-Soares P., 2004, AJ, 128, 47
Fan J., Xiao H., Yang W., Zhang L., Strigachev A. A., Bachev R. S., Yang J., 2023, ApJS, 268, 23
Fan J.-H. et al., 2008, PASJ, 60, 707
Fan Z.-H., Cao X., 2004, ApJ, 602, 103
Foschini L., Ghisellini G., Tavecchio F., Bonnoli G., Stamerra A., 2011, A&A, 530, A77
Franckowiak A. et al., 2020, ApJ, 893, 162
Gao S., Pohl M., Winter W., 2017, ApJ, 843, 109
Garrappa S. et al., 2019, ApJ, 880, 103
Gasparyan S., Bégué D., Sahakyan N., 2022, MNRAS, 509, 2102
Gehrels N. et al., 2004, ApJ, 611, 1005
Ghisellini G., Madau P., 1996, MNRAS, 280, 67
Ghisellini G., Maraschi L., 1989, ApJ, 340, 181
Ghisellini G., Tavecchio F., 2008, MNRAS, 387, 1669
Ghisellini G., Tavecchio F., Foschini L., Ghirlanda G., 2011, MNRAS, 414, 2674
Giommi P., Glauch T., Padovani P., Resconi E., Turcati A., Chang Y. L., 2020a, MNRAS, 497, 865
Giommi P., Padovani P., Oikonomou F., Glauch T., Paiano S., Resconi E., 2020b, A&A, 640, L4
HI4PI Collaboration, 2016, A&A, 594, A116
Hewett P. C., Wild V., 2010, MNRAS, 405, 2302
Hu X.-K., Yu Y.-W., Zhang J., Wu T.-Z., Lian J.-S., Wang X.-G., Zhang H.-M., Liang E.-W., 2024, ApJ, 963, L41
IceCube Collaboration, 2024, GRB Coordinates Network, 35485, 1
IceCube Collaboration, 2018a, Science, 361, 147
IceCube Collaboration, 2018b, Science, 361, eaat1378
Jin Y. K., Zhang S. N., Wu J. F., 2008, ApJ, 678, 563
Kadler M. et al., 2016, Nat. Phys., 12, 807
Kelner S. R., Aharonian F. A., 2008, Phys. Rev. D, 78, 034013
Khatoon R., Boettcher M., Robinson J., 2026, ApJ, 999, 245
Kiehlmann S., Hovatta T., Kadler M., Max-Moerbeck W., Readhead A. C. S., 2019, Astron. Telegram, 12996, 1
Kim D.-W., Ros E., Kadler M., Krichbaum T. P., Zhao G.-Y., Rösch F., Lobanov A. P., Anton Zensus J., 2024, A&A, 692, A203
Konigl A., 1981, ApJ, 243, 700
Kouch P. M. et al., 2024, A&A, 689, A119
Kun E., Bartos I., Tjus J. B., Biermann P. L., Halzen F., Mező G., 2021, ApJ, 911, L18
Kushwaha P. et al., 2018, MNRAS, 473, 1145
Liodakis I., Romani R. W., Filippenko A. V., Kiehlmann S., Max-Moerbeck W., Readhead A. C. S., Zheng W., 2018, MNRAS, 480, 5517
Liodakis I., Romani R. W., Filippenko A. V., Kocevski D., Zheng W., 2019, ApJ, 880, 32
Mannheim K., 1993, A&A, 269, 67
Mannheim K., Biermann P. L., 1992, A&A, 253, L21
Marscher A. P., Gear W. K., 1985, ApJ, 298, 114
Mattox J. R. et al., 1996, ApJ, 461, 396
Melia F., Konigl A., 1989, ApJ, 340, 162
Miller H. R., Carini M. T., Goodrich B. D., 1989, Nature, 337, 627
Morton T. et al., 2008, Astron. Telegram, 1661, 1
Murphy M. T., Kacprzak G. G., Savorgnan G. A. D., Carswell R. F., 2019, MNRAS, 482, 3458
Noble J. C., Miller H. R., 1994, BAAS, 26, 797
Nolan P. L. et al., 2012, ApJS, 199, 31
Oikonomou F., Petropoulou M., Murase K., Tohuvavohu A., Vasilopoulos G., Buson S., Santander M., 2021, J. Cosmol. Astropart. Phys., 2021, 082
Omeliukh A. et al., 2025, A&A, 695, A266
Padovani P., Giommi P., Resconi E., Glauch T., Arsioli B., Sahakyan N., Huber M., 2018, MNRAS, 480, 192
Paiano S., Falomo R., Treves A., Scarpa R., 2018, ApJ, 854, L32
Paiano S., Falomo R., Treves A., Scarpa R., Sbarufatti B., 2024, ApJ, 968, 81
Pandey A., Stalin C. S., 2022, A&A, 668, A152
Pandey A., Rajput B., Stalin C. S., 2022, MNRAS, 510, 1809
Petropoulou M. et al., 2020, ApJ, 891, 115
Poole T. S. et al., 2008, MNRAS, 383, 627
Prince R., Das S., Gupta N., Majumdar P., Czerny B., 2024, MNRAS, 527, 8746
Rajput B., Stalin C. S., Sahayanathan S., Rakshit S., Mandal A. K., 2019, MNRAS, 486, 1781
Rajput B., Shah Z., Stalin C. S., Sahayanathan S., Rakshit S., 2021, MNRAS, 504, 1772
Rajput B., Pandey A., Stalin C. S., Mathew B., 2022, MNRAS, 517, 3236
Rakshit S., Stalin C. S., Muneer S., Neha S., Paliya V. S., 2017, ApJ, 835, 275
Rodrigues X., Garrappa S., Gao S., Paliya V. S., Franckowiak A., Winter W., 2021, ApJ, 912, 54
Rodrigues X., Paliya V. S., Garrappa S., Omeliukh A., Franckowiak A., Winter W., 2024, A&A, 681, A119
Roming P. W. A. et al., 2005, Space Sci. Rev., 120, 95
Sahakyan N., Giommi P., Padovani P., Petropoulou M., Bégué D., Boccardi B., Gasparyan S., 2023, MNRAS, 519, 1396
Sahakyan N. et al., 2024a, AJ, 168, 289
Sahakyan N., Harutyunyan G., Gasparyan S., Israyelyan D., 2024b, MNRAS, 528, 5990
Sahayanathan S., Godambe S., 2012, MNRAS, 419, 1660
Saito S., Stawarz Ł., Tanaka Y. T., Takahashi T., Madejski G., D'Ammando F., 2013, ApJ, 766, L11
Scarpa R., Falomo R., 1997, A&A, 325, 109
Schlafly E. F., Finkbeiner D. P., 2011, ApJ, 737, 103
Shaw M. S. et al., 2012, ApJ, 748, 49
Shen Y. et al., 2011, ApJS, 194, 45
Sikora M., Begelman M. C., Rees M. J., 1994, ApJ, 421, 153
Smith P. S., Williams G. G., Schmidt G. D., Diamond-Stanic A. M., Means D. L., 2007, ApJ, 663, 118
Stathopoulos S. I., Petropoulou M., Vasilopoulos G., Mastichiadis A., 2024, A&A, 683, A225
Stocke J. T., Morris S. L., Gioia I. M., Maccacaro T., Schild R., Wolter A., Fleming T. A., Henry J. P., 1991, ApJS, 76, 813
Taboada I., Stein R., 2019, Astron. Telegram, 12967, 1
Tavecchio F., Ghisellini G., Bonnoli G., Ghirlanda G., 2010, MNRAS, 405, L94
Ulrich M.-H., Maraschi L., Urry C. M., 1997, ARA&A, 35, 445
Vaughan S., Edelson R., Warwick R. S., Uttley P., 2003, MNRAS, 345, 1271
Vlasyuk V. V. et al., 2024, MNRAS, 535, 2775
Wagner S. J., Witzel A., 1995, ARA&A, 33, 163
Wang Z.-J., Liu R.-Y., Wang Z.-R., Wang J., 2024, ApJ, 962, 142
Zhang H., Böttcher M., 2013, ApJ, 774, 18
Zhang H., Böttcher M., Liodakis I., 2024, ApJ, 967, 93

This paper has been typeset from a TEX/LATEX file prepared by the author.